

Cold Molecular Gas in the Inner Two Kiloparsec of NGC 4151¹

G. Dumas

Max-Planck-Institut für Astronomie, Königstuhl 17, D-69117 Heidelberg, Germany

E. Schinnerer

Max-Planck-Institut für Astronomie, Königstuhl 17, D-69117 Heidelberg, Germany

C.G. Mundell

*Astrophysics Research Institute, Liverpool John Moores University, Twelve Quays House,
Egerton Wharf, Birkenhead, CH41 1LD, UK*

ABSTRACT

We present the first spatially resolved spectroscopic imaging observations of the ^{12}CO (1-0) line emission in the central 2.5 kpc of the Seyfert 1 galaxy NGC 4151, obtained with the IRAM Plateau de Bure Interferometer (PdBI). Most of the cold molecular gas is distributed along two curved gas lanes about 1 kpc north and south of the active nucleus, coincident with the circumnuclear dust ring noted by previous authors. These CO arcs lie within the Inner Lindblad Resonance of the large scale oval bar and have kinematics consistent with those derived from neutral hydrogen observations of the disk and bar. Two additional gas clumps are detected that show non-circular motions - one associated with the southern gas lane and one lying ~ 600 pc north of the nucleus. Closer to the nucleus, no cold molecular gas is detected in the central 300 pc where abundant near-IR H_2 line emission arises. This suggests that the H_2 line emission is not a good indicator for a cold gas reservoir in NGC 4151 and that the H_2 is likely photo-excited by the AGN. The upper limit of the CO mass in the central 300 pc is sufficient to support the AGN activity at its current level for 10^7 yrs. The total cold molecular mass detected by PdBI is $4.3 \times 10^7 M_\odot$. Finally, 3 mm continuum emission arising from the location of the AGN is detected with a flux of $S_{3\text{mm}} \sim 14$ mJy and appears to be unresolved at an angular resolution of $2''.8$ (~ 180 pc).

Subject headings: galaxies: Seyfert – galaxies: ISM – galaxies: kinematics and dynamics – galaxies: individual(NGC 4151)

1. Introduction

Nuclear activity in galaxies is thought to be driven by the release of gravitational potential energy from material accreted by a central supermassive black hole. In this scenario, fuel transportation mechanisms in the nuclear regions must be efficient on time scales comparable to that of the nuclear activity of the order of 10^7 - 10^8 yrs (e.g. Martini 2004; Marconi et al. 2004). Stellar bars are well known to drive gas from the outer large-scale disk to the central kiloparsec (Sakamoto et al. 1999; Sheth et al. 2005) and the bar-within-bar scenario (Shlosman et al. 1989) was proposed as a mechanism to deliver gas closer to the central black hole. Recently, other gravitational perturbations, such as $m=1$ modes or gas density waves, have been suggested to play a major role in the transport of gas to the most central regions (e.g. Englmaier & Shlosman 2000; Emsellem 2001; García-Burillo et al. 2003a).

Molecular gas dominates the interstellar medium (ISM) in the centers of nearby spiral galaxies, therefore CO lines are the best tracers for the nuclear gas distribution and dynamics. High resolution CO observations of the central kpc regions of nearby active galaxies provide insights on the ISM properties in these regions and the processes that could move gas inwards. The recently completed NUGA survey with the IRAM mm-interferometer PdBI (Plateau de Bure interferometer) (García-Burillo et al. 2003a) observed 12 Seyfert and LINER galaxies with different nuclear and host properties and showed that molecular gas is present in the centers, however with diverse morphology and kinematics. This already suggests that more than one single mechanism acting in the central kpc might be responsible for fueling the black hole (García-Burillo et al. 2003a, 2005; Combes et al. 2004; Krips et al. 2005; Boone et al. 2007; Hunt et al. 2008; Lindt-Krieg et al. 2008; Casasola et al. 2008; Haan et al. 2009; Combes et al. 2009). Thus, the mechanism for transporting material from the central few hundred pc to the SMBH in order to induce and sustain the nuclear activity remains debated. Observations of molecular gas in nearby AGN can begin to bridge this gap, connecting large and small spatial scales and examining the next link in the fueling chain. In this context, the nearby spiral galaxy NGC 4151 hosting a Seyfert 1 nucleus is an ideal target.

NGC 4151 is one of the best studied Active Galactic Nuclei (AGN) (see review by Ulrich 2000) and situated at a distance of 13.3Mpc ($1'' = 65$ pc, Mundell et al. 2003). It is a barred spiral galaxy, classified as (R')SAB(rs)ab (de Vaucouleurs et al. 1991), and seen nearly face-on ($i=21^\circ$). In addition to a remarkably large stellar bar ($3' \times 2' \approx 11.7$ kpc \times 7.8 kpc), two faint spiral arms extend out to a radius of $\sim 6'$ (23.4 kpc). It has been extensively observed at all wavelengths and on various spatial scales. In particular neutral hydrogen (H I) traces the

¹Based on observations carried out with the IRAM Plateau de Bure Interferometer. IRAM is supported by INSU/CNRS (France), MPG (Germany) and IGN (Spain).

large-scale stellar bar and the outer spiral arms. On kpc scales, Vila-Vilaro et al. (1995) have detected two red arc-like features, possibly produced by dust extinction of the background stellar continuum, which delineate a circumnuclear elliptical ring (hereafter: central dust ellipse) with a semi-major axis of $\sim 18''$ (~ 1.2 kpc). In addition a large Extended Narrow Line Region (ENLR) extends up to $20''$ (1.3 kpc) and is consistent with ambient galactic gas being photo-ionized by a cone of nuclear UV radiation (Penston et al. 1990). Evidence for radial outflow have been observed and modelled in the NLR of NGC4151 (Heckman & Balick 1983; Schulz 1990; Hutchings et al. 1998; Kaiser et al. 2000; Crenshaw et al. 2000; Das et al. 2005; Storchi-Bergmann et al. 2010). The bright Seyfert nucleus of type 1.5 displays rapid optical variability, and a small ~ 600 pc long radio jet at a position angle (PA) of $\sim 80^\circ$ (Pedlar et al. 1993). On scales of about $1''$ to $2''$, optical CCD imaging revealed evidence for obscuration in the form of a reddened band of enhanced extinction (or low ionization) crossing the central region, and aligned approximately perpendicular to the ENLR and radio jet (Perez et al. 1989; Terlevich et al. 1991). In addition, there is also evidence of neutral gas and dust within ~ 10 pc of the nucleus (Mundell et al. 1995, 1999). A summary of the properties of NGC4151 is provided in Tab. 1.

Here we present the first mm-interferometric $^{12}\text{CO}(1-0)$ observations of the central 2 kpc of NGC4151, encompassing the dust ellipse, obtained with PdBI. These data provide a link between the large-scale bar and the (putative) torus seen in HI in absorption (Mundell et al. 2003). We describe the observations and data reduction in Sect. 2. The resulting CO maps and molecular gas properties are presented in Sect. 3. The relation between the molecular gas and the large-scale properties of NGC4151 is analyzed in Sect. 4.1. In Sect. 4.2, cold and warm molecular gas properties in the innermost region are compared and we discuss our results in the context of AGN fueling in Sect. 4.3. Finally we conclude in Sect.5.

2. Observations and Data Reduction

The $^{12}\text{CO}(1-0)$ emission line at 3mm was observed with IRAM/PdBI using 6 antennas in C and D configuration on December 26 and 27, 2008 and April 9 and 19, 2009, respectively, providing baselines from 24 m to 176 m. The calibration and mapping were done with the standard IRAM GILDAS software packages CLIC and MAPPING (Guilloteau & Lucas 2000). The phase center of the observation was at RA= $12^h 10^m 32.^s 579$ and DEC= $+39^\circ 24' 20''.63$ in the J2000.0 coordinate system, all velocities are observed relative to $v_{sys} = 995 \text{ km s}^{-1}$. The quasars 3C273, 3C84, 3C345, 1144+402, 1308+326, 0923+392, 0528+134 and 1156+295 were observed as flux calibrators. During all observations, 1144+402 was used as phase calibrator and observed every 24min.

We separately calibrated each day of observations using the corresponding phase and flux calibrators. All observations were then merged into a single dataset. The correlator was set to a spectral resolution of 1.25MHz per channel, corresponding to a velocity resolution of 3.25 km s⁻¹. We binned by two channels for a final spectral resolution of 6.5 km s⁻¹. In addition, a pure continuum map was created by averaging all channels with no line emission. In order to obtain a data cube containing only emission line information, the continuum was subtracted from the line data in the *uv*-plane using the task UV_SUBTRACT in GILDAS. The continuum and emission line only data were cleaned separately, using uniform and natural weighting (see Tab. 2). All cleaned data have a pixel size of 0.5'', with an image size of 256×256 pixels .

The channel maps of the naturally weighted CO(1-0) line are presented in Fig. 1 along with the dirty beam and the *uv* coverage. All data are presented without primary-beam correction applied. At the observed frequency, the typical FWHM of the PdBI primary beam is 44''. Hereafter, we present the continuum emission at the uniform resolution (2.83''×2.16'') and the results from the naturally weighted emission line cube at 6.5 km s⁻¹ velocity resolution, which has a lower spatial resolution (beam of 3.44''×2.96'' or 224pc×192pc) but a better sensitivity, with a noise level of 2 mJy beam⁻¹, than the uniformly weighted cube (for which the rms is 2.8 mJy beam⁻¹).

3. Continuum, Molecular Gas Distribution and Kinematics

Here we present the properties of the mm continuum and CO(1-0) line emission in the central two kpc of NGC4151, as observed with PdBI.

3.1. Millimeter continuum emission

The cleaned millimeter continuum map derived with uniform weighting is shown in Fig. 2. The beam size is 2.8''×2.2'' and the rms noise is 0.3 mJy beam⁻¹. The total integrated flux density is 14 mJy and the peak flux is 12 mJy beam⁻¹. The millimeter continuum peaks at RA= 12^h10^m32.^s56 and DEC= +39°24'21''06 (J2000.0) corresponding to the AGN location (Mundell et al. 2003), with an offset of 0.25'', consistent with our astrometric uncertainty of about 0.4''. At this resolution it is barely resolved: a two-dimensional Gaussian fit gives a convolved source size of 3.2''×2.3'' with a PA of 93°. While the elongation of the continuum is similar to the shape of the clean beam, this suggests a small extent in east-west direction roughly consistent with the orientation of the radio jet that is elongated along a

PA of 77° (Mundell et al. 1995).

3.2. CO line emission

We used the task MOMENTS in GIPSY to construct the intensity, velocity and velocity dispersion maps of the CO(1-0) line emission, using a flux clipping level of $3\sigma=6 \text{ mJy beam}^{-1}$ per channel and considering emission only as real if it appears at least in two consecutive channels. The width of 2 channels is 13 km s^{-1} , smaller than the typical line width (20 km s^{-1}) seen throughout the data cube. The three moment maps of the naturally weighted data cube are shown in Fig. 3.

3.2.1. Molecular gas morphology and masses

The integrated intensity map of the CO line emission (Fig. 3, top panel) shows a fairly regular geometry. About $15''$ north and south of the nucleus the molecular gas forms two gas lanes that run roughly in east-west direction over a length of $16''$ (north) and $20''$ (south). The southern lane is about twice as bright than the northern lane. In addition to these extended structures, several fainter and more compact clumps are detected. All major components are indicated in Fig. 4. The most prominent clump is closest to the nucleus (labeled as central clump in Fig. 4) at a distance of $9''$ ($\approx 600 \text{ pc}$) to the North. Four additional smaller clumps are present, three near the northern lane and the last one at about $25''$ west (western clump on Fig 4) of the center of NGC4151.

We measured the CO fluxes within different components marked in Fig. 4 using the tasks BLOT (to define the regions) and FLUX in GIPSY. All the fluxes presented here are corrected for primary beam attenuation. We then converted the CO(1-0) flux into molecular gas mass for each component, using a standard Galactic CO-to- H_2 conversion factor of $X_{\text{CO}} = 2 \times 10^{20} \text{ cm}^{-2} [\text{K km s}^{-1}]^{-1}$ (Solomon & Barrett 1991) and applying a mass correction for helium of 36%. The derived CO fluxes and molecular gas masses are listed in Tab. 3. In our entire map, the total flux recovered is $14.7 \text{ Jy km s}^{-1}$ and the corresponding cold molecular gas mass is about $4.3 \times 10^7 M_\odot$, with 60% of this mass being contained in the southern lane. Our PdBI data recover more flux than the JCMT single dish measurements (Rigopoulou et al. 1997). They measure a total CO(2-1) flux of $I_{\text{CO}} = 1.56 \text{ K km s}^{-1}$, corresponding to $S_{\text{CO}(1-0)} = 11 \text{ Jy km s}^{-1}$ in integrated flux, assuming optically thick molecular gas, in the inner $23''$ ($\sim 1.5 \text{ kpc}$). The total H_2 mass derived from the single dish data is then $M(\text{H}_2) = 2.4 \times 10^7 M_\odot$ which corresponds to a total molecular mass of $M_{\text{mol}} = 3.2 \times 10^7 M_\odot$, after applying the mass

correction for helium. Therefore, the JCMT data missed about 25% of flux coming from the outer edge of the CO gas lanes.

Interestingly, we detect no CO emission in the central $3''$, where warm H_2 emission is observed via its NIR emission lines (Fernandez et al. 1999; Storchi-Bergmann et al. 2009). We discuss the discrepancy between the CO and NIR H_2 observations in the central regions in Sect. 4.2.

3.2.2. CO kinematics

The CO(1-0) velocity field and the velocity dispersion map are presented in the middle and bottom panels of Fig. 3. The velocity field in the extended southern and northern lanes shows an ordered gradient along the lanes with values similar to those derived from HI observations (Asif et al. 1998; Mundell et al. 1999) and an average velocity dispersion of approximately 7 km s^{-1} . Fig. 5 shows the integrated spectra of the three main components: the northern and southern gas lanes as well as the central clump. The integrated spectrum of the northern lane is centered on 80 km s^{-1} and the central clump at 55 km s^{-1} . The spectrum of the southern lane shows the presence of two kinematic components originating from each half of the lane - one centered on 0 km s^{-1} , corresponding to the eastern part of the lane where it curves to the North, and the other centered on -40 km s^{-1} arising from its most prominent western part - separated by a region in the centre of the lane that shows an increased velocity dispersion, close to the kink point. Fig. 6 shows a selection of spectra taken close to this high velocity dispersion region. Asymmetry in the line profiles is clear, suggesting multiple kinematic components, but this region is spatially only marginally resolved while a second line component can be easily identified in several spectral. This boundary region between the two halves of the gas lane therefore may represent a region in which gas clouds with distinct velocities overlap along the line of sight or a genuinely mixed, disturbed zone. Larger velocity dispersion in the east part of the northern lane may also indicate that the eastern part of this lane is a distinct cloud and although the line profiles in this region deviate from a simple Gaussian shape they show no clear evidence of two components in this region.

We extracted pv diagrams along three different positions that are presented in Fig. 7. The pv diagram along the major kinematic axis of $PA=22^\circ$ shows strong emission from the gas lanes at $+80 \text{ km s}^{-1}$ and -50 km s^{-1} . The CO(1-0) line emission shows a velocity gradient indicating that the gas is participating in circular motion. Interestingly this gradient is not symmetric with respect to the systemic velocity of 995 km s^{-1} from Pedlar et al. (1992), it presents an offset of $+15 \text{ km s}^{-1}$. In order to investigate the gas motion within the gas lanes two slits were placed along them (number 2 and 3, Fig. 7). While the velocity gradient is very

low in the northern lane with a mean velocity of about $+80 \text{ km s}^{-1}$, two distinct features are present in the southern lane. The eastern part of the lane shows constant velocities consistent with the systemic velocity, the western part exhibits a clear velocity gradient from -20 to -60 km s^{-1} .

The CO(1-0) rotation curve of NGC4151 was derived from the velocity field using the task ROTCUR in GIPSY. This task fits the velocity, assumed to be circular, within tilted rings. We run ROTCUR for rings of $2''$ widths from $3''$ to $19''$ radial distances centered on the AGN as traced by the peak of the 3mm continuum. The region defined by an angle of 5° around the minor axis was excluded for the fit. The inclination and position angle were fixed at $i=21^\circ$ and $PA=22^\circ$ as derived from the HI data by Mundell et al. (1999). The systemic velocity, v_{sys} , was allowed to vary in a first step and found to be at 1010 km s^{-1} , i.e. offset by about $+15 \text{ km s}^{-1}$ from the value derived by Pedlar et al. (1992). This offset is consistent with the offset in the velocity gradient along the major axis, as discussed above. Indeed, with a systemic velocity of 1010 km s^{-1} , the pv diagram along the major kinematic axis ($PA=22^\circ$) presents a more symmetric velocity gradient, the southern and northern CO lanes lying then at -65 and $+65 \text{ km s}^{-1}$, respectively.

The resulting rotation curve, extracted with $v_{sys} = 1010 \text{ km s}^{-1}$ is presented in Fig. 8. The point at $9''$ presents a velocity lower than expected for circular rotation. This point corresponds to the north-eastern part of the southern lane, which has been shown to have kinematics distinct from the west part of the lane (Fig. 5). The low velocity of the first point at $3''$ is due to beam smearing. Comparison to the HI rotation curve (Mundell et al. 1999) shows a good agreement between the CO and HI rotation curves (Fig. 8, right).

Therefore the overall CO kinematics are generally consistent with rotation in the plane of the galaxy. To demonstrate this further, Fig. 9 shows velocity as a function of position angle measured directly along the CO arcs. The sinusoidal curves overplotted show the expected variation of velocity along a circular annulus in the plane of the galaxy ($i=21^\circ$, $PA=22^\circ$) at a radius of $18''$ corresponding to the semi-major axis of the dust/CO ellipse. Although not exact, the correspondence between the plotted curves is good, ruling out the interpretation that the ellipticity traced by the CO arcs is a result of gas lying in a highly inclined circular disk tilted out of the main galactic plane as well as strong non-circular motions within the disk. The morphology is therefore intrinsically elliptical in the plane of the galaxy, as suggested by the analysis of the HI velocities along the dust arcs (Fig.3 of Asif et al. 1998) and consistent with predictions of gas flows in bars (Athanasoula 1992). The rotation curve in Fig. 8 is thus only an approximation to the true kinematics and the offset between the derived CO and HI systemic velocities is a likely indication of disturbed CO gaseous kinematics in these arcs.

Finally, the velocities within the central clump present larger deviations from circular motions, up to 50 km s^{-1} below the circular velocity at a radius of $5''$ (Fig. 9, right). The central clump shows redshifted kinematics (see Fig. 3) significantly inconsistent with those expected for circular motion in this region, close to the minor kinematic axis of the galaxy. These observed deviations are suggestive of streaming motions, however, the uncertainties are too large to derive a more quantitative measure. Very deep CO imaging in the future is required to confirm whether this clump is an isolated cloud or part of a more continuous fluid flow towards the nucleus.

4. Discussion

4.1. Role of the Large-Scale Stellar Bar

In order to analyse the importance of the large-scale stellar bar or oval for fueling the AGN, we need to establish the link between the bar and the molecular gas observed in the central 2.5 kpc. The detailed HI study of Mundell & Shone (1999) showed that the stellar bar/oval is unusually gas-rich and that its HI gas dynamics are consistent with the presence of x_2 orbits in an oval bar: sharp velocity changes across the bright regions close to the leading edges of the bar are found which can be explained by offset shocks predicted by simulations (Athanasoula 1992) and provide direct evidence for the presence of these x_1 and x_2 families of stellar orbits. The $\text{H}\alpha$ image (Knapen et al. 2004) reveals HII regions along the leading sides of the large-scale oval coincident with the peaks in the HI surface density. These HII regions are associated with the ionized and neutral gas in the streaming shocks (Asif et al. 2005) that connect to the CO gas lanes to form an inner gaseous spiral (Fig. 10, left). Mundell et al. (1999) derived the resonance curves from the HI velocity field and estimated the Inner Lindblad Resonance (ILR) to be at 2.8 ± 0.6 kpc. The ILR (red circle in Fig. 10, left) coincides with the HII regions, while the CO lanes are well inside the resonance. This picture is consistent with the molecular gas tracing a spiral density wave, driven by the large scale bar and extending from the ILR down to the center (Englmaier & Shlosman 2000). As we do not detect CO all the way down to the nucleus, this may argue in favor of the presence of a second ILR that limits the gaseous wave to exist between the two resonances (Englmaier & Shlosman 2000). However, the sparse distribution of the CO gas, the lack of HI in the central regions and the non-linear behaviour of gas in a barred potential prevent useful constraints on the presence and location of an inner ILR from being derived directly from the gaseous rotation curves. Full dynamical modelling and numerical simulations constrained by millimetre, radio and optical velocity fields and K-band derived mass models will be presented in a future paper (Dumas et al. in prep.) and may

provide insight into location of an inner ILR and its effect on the gas dynamics.

The CO gas lanes also coincide with two dust lanes seen in a V-I color map (Asif et al. 1998), as shown in Fig. 10, right. The two red arcs delineate a $11'' \times 18''$ dust ellipse inside the large oval/bar and also coincide with HI emission (Asif et al. 1998). The peak column densities in the HI arcs are $(0.7 - 1.8) \times 10^{21} \text{ cm}^{-2}$ implying an atomic gas mass of $M_{\text{HI}} \sim (0.13 - 3.3) \times 10^6 M_{\odot}$. Thus the ratio of atomic to molecular gas is 0.3 in the northern lane and 0.006 in the southern lane, which is in agreement with the values of the atomic-to-molecular gas ratio observed in the central regions of spiral galaxies (Schuster et al. 2007; Leroy et al. 2008), with the southern lane being at the lower end. Moreover, the kinematics of the CO gas lanes and the HI arcs are in good agreement as shown in the previous section. Therefore the morphology and kinematics of the CO northern and southern lanes suggest that the molecular gas lanes are the continuation of the atomic and dusty ring, along elliptical orbits of the stellar bar.

It is interesting to note that while the structure of the gas lanes is very well matched, no obvious counter-structure is present in the V-I map for the nuclear clump. High resolution HST/ACS imaging shows the presence of dust in the central 1.5 kpc, but no clear structure is seen in the dust (Bentz et al. 2006). Connecting the gas flows in the large scale bar with the nuclear dust structures therefore remains a challenge.

4.2. Cold and warm molecular gas in the innermost region

In the central $2''.5$, excited H_2 line emission centered on the nucleus and extended along the minor axis of the galaxy ($0''.8 \approx 50 \text{ pc}$) has been observed by Fernandez et al. (1999) and more recently by Storchi-Bergmann et al. (2009). The latter showed that H_2 is thermally excited either by X-rays from the AGN or by shocks along the accretion flow towards the nucleus. This central H_2 emission has been interpreted as tracing the reservoir of (cold) gas from which the super-massive black hole in NGC 4151 is being fed. In particular, Storchi-Bergmann et al. (2009) found a mass of hot H_2 gas of $240 M_{\odot}$ and based on the conversion of warm-to-cold H_2 mass ranging between 10^{-7} and 10^{-5} (Dale et al. 2005), they estimated the total mass of molecular gas (hot plus cold) to be in the range of $2.4 \times 10^7 - 10^9 M_{\odot}$. We should easily have detected such an amount of molecular gas. Indeed, the 1σ upper limit for the CO(1-0) emission within the central $3''$ is $0.033 \text{ Jy km s}^{-1}$, which translates into a limit for the cold molecular gas mass of $10^5 M_{\odot}$, well below the lower limit expected from the NIR H_2 line.

This discrepancy between warm and cold molecular gas mass can be interpreted in two

opposite ways. On one hand, it indicates that no significant amount of cold molecular gas is present close to the nucleus. This implies that the warm molecular gas observed there is not a good tracer for the general amount of (cold) molecular gas present. Thus the use of a generalized ratio of warm-to-cold H_2 could be misleading in the vicinity of AGN, which would explain the large over-estimate of cold molecular gas mass by Storchi-Bergmann et al. (2009). On the other hand, in X-rays dominated regions (XDR), equilibrium molecular abundances may be affected by the X-rays radiation from the AGN. This leads in particular to a depletion of CO abundance with respect to other molecules such as HCN (Boger & Sternberg 2005). Indeed many Seyfert galaxies show enhanced central HCN(1-0) emission such as, e.g. NGC1068 (Jackson et al. 1993; Tacconi et al. 1994; Helfer & Blitz 1995; Usero et al. 2004), NGC1097 (Kohno et al. 2003), NGC5194 (Kohno et al. 1996), NGC6951 (Krips et al. 2007a). In particular, the latter study showed that the CO line emission largely underestimates the amount of cold molecular gas in the central region of the Seyfert 2 NGC6951. Therefore, CO itself may be a poor tracer of cold molecular gas close to an active nucleus. Under this assumption, the change of chemistry in the central kpc because of the AGN itself could explain the lack of CO emission inside the dust/gas lanes and the excitation of the NIR H_2 would be then driven by the AGN rather than the accretion flow. Further study of molecular abundances in the central $3''$ of NGC4151 are needed to quantify the cold molecular mass in the central region of NGC4151 and to explain this discrepancy between (cold) molecular gas masses inferred from NIR H_2 and CO line emission.

4.3. Implication for AGN fueling

The presence of non-circular motions in the central clump indicates that fueling of the AGN or at least a replenishment of the gas reservoir closer to the AGN might be ongoing. Analysis of near-IR images reveal no evidence for a second inner stellar bar (Onken et al. 2007). This suggests that the disturbances of the regular motions might be caused by a transient event, such as an interaction with a nearby galaxy. Such an interaction has been proposed by Mundell et al. (1999) to explain the distortion of the large two-arm stellar spiral. NGC4156 and UGC07188 have small projected distances to NGC4151 and therefore may be candidate companions for such a galaxy interaction, although at respectively $v_{sys}=6750 \text{ km s}^{-1}$ and 6850 km s^{-1} the systemic velocities of NGC4156 and UGC07188 are significantly larger than that of NGC4151.

Our findings are in agreement with recent results from the NUGA survey that found no direct indication for ongoing fueling within the central hundred of parsecs for most of their targets (García-Burillo et al. 2005; Boone et al. 2007; Lindt-Krieg et al. 2008; Casasola et al.

2008; Haan et al. 2009). It is, however, interesting that most NUGA galaxies have a molecular gas reservoir within the inner kiloparsec with mass between $10^7 - 10^{10} M_{\odot}$ (García-Burillo et al. 2003b; Combes et al. 2004; García-Burillo et al. 2005; Krips et al. 2005; Boone et al. 2007; Krips et al. 2007b; Casasola et al. 2008; García-Burillo et al. 2009; Combes et al. 2009). It is also interesting to note that most NUGA targets are either Seyfert type 2 or LINER galaxies. While gravitational mechanisms, driven e.g. by large scale stellar bars or galaxy interaction, are efficient in transporting gas to the central kpc of galaxies, other processes (e.g. viscous torques, García-Burillo et al. 2005; Haan et al. 2009) must take over to bring the gas closer to the nucleus and fuel the AGN. Moreover, recent nuclear star formation and AGN activity have been shown to be linked (González Delgado et al. 2001; Riffel et al. 2007; Davies et al. 2007), and stellar outflows, from starburst on tens of parsec scales, can also support the nuclear activity (Davies et al. 2007; Hicks et al. 2009; Schartmann et al. 2009). NGC4151 presents no evidence for a recent nuclear starburst (Sturm et al. 1999). In fact, the star formation rate across the whole galaxy is unusually low given the presence of significant quantities of HI gas (Asif et al. 2005), therefore this scenario appears to be unlikely for this particular Seyfert galaxy. Finally, Dumas et al. (2007) showed that the ionised gaseous kinematics of Seyferts are more disturbed with respect to the stellar kinematics in the central kiloparsec than those of inactive galaxies, i.e. that kinematic disturbance scales with accretion rate in the inner kiloparsec where dynamical and activity timescales become comparable.

5. Summary and Conclusions

We have presented the first interferometric map of the molecular gas reservoir in NGC 4151 using PdBI. A total molecular gas mass of $4.3 \times 10^7 M_{\odot}$ is detected in the central 2.5 kpc. Most of the gas is located in two gas lanes at 1 kpc distance from the nucleus. A nuclear clump containing about 3% of the total mass is found 600 pc north of the nucleus. However, no CO emission associated with the AGN has been detected down to a limit of $10^5 M_{\odot}$ for the central $3''$ indicating that estimates of the cold gas reservoir based on NIR H_2 line emission, based on the assumption of the ro-vibrational H_2 emission line in thermal equilibrium, can lead to severe overestimation of the amount of total gas present.

The morphology and kinematics of the gas lanes are consistent with being driven by the large-scale stellar bar and also coincide with dust lanes seen in optical color maps. The detection of non-circular inward motion in the nuclear clump suggests that this cloud may trace gas that will ultimately flow towards the SMBH. However, the kinematics of the central clump could not be linked directly to those induced by the large-scale stellar bar. Detailed

dynamical modeling of the gravitational potential of the bar and the inner kpc regions is required to combine the molecular and ionised gas and stellar components in a coherent framework and identify the mechanism responsible for the observed non-circular motions, which is beyond the scope of this paper. Thus we speculate here that the potential inflow is caused by a transient phenomenon and the fueling process of the AGN might be erratic and intermittent. In agreement with recent studies of other nearby AGN, these findings suggest that no single (gravitational) mechanism is responsible for the fueling of nuclear activity. Finally, in the central kpc where dynamical and activity timescales become comparable, a fine balance may be required between fueling and feedback, but in NGC4151, which has an estimated accretion rate of $\dot{m} = 1.3 \times 10^{-2} M_{\odot} \text{yr}^{-1}$ (Storchi-Bergmann et al. 2010), the upper limit on cold molecular gas in the central $3''$ ($10^5 M_{\odot}$) given by our CO observations is still sufficient to support the current level of activity of NGC4151 over an AGN lifetime of 10^7yr .

We would like to thank the staff on the Plateau de Bure for doing the observations and Philippe Salome for his help with the IRAM data reduction. We also are thankful to Witold Maciejewski for fruitful discussions and to the anonymous referee for useful comments that helped to improve this paper. CGM acknowledges financial support from the Royal Society and Research Councils U.K. GD was supported by DFG grants SCH 536/4-1 and SCH 536/4-2 as part of SPP 1177.

Facilities: IRAM (PdBI).

REFERENCES

- Asif, M. W., Mundell, C. G., & Pedlar, A. 2005, MNRAS, 359, 408
- Asif, M. W., Mundell, C. G., Pedlar, A., Unger, S. W., Robinson, A., Vila-Vilaro, B., & Lewis, J. R. 1998, A&A, 333, 466
- Athanassoula, E. 1992, MNRAS, 259, 328
- Bentz, M. C., Peterson, B. M., Pogge, R. W., Vestergaard, M., & Onken, C. A. 2006, ApJ, 644, 133
- Boger, G. I., & Sternberg, A. 2005, ApJ, 632, 302
- Boone, F., Baker, A. J., Schinnerer, E., Combes, F., García-Burillo, S., Neri, R., Hunt, L. K., León, S., Krips, M., Tacconi, L. J., & Eckart, A. 2007, A&A, 471, 113

- Casasola, V., Combes, F., García-Burillo, S., Hunt, L. K., León, S., & Baker, A. J. 2008, *A&A*, 490, 61
- Combes, F., Baker, A. J., Schinnerer, E., García-Burillo, S., Hunt, L. K., Boone, F., Eckart, A., Neri, R., & Tacconi, L. J. 2009, *A&A*, 503, 73
- Combes, F., García-Burillo, S., Boone, F., Hunt, L. K., Baker, A. J., Eckart, A., Englmaier, P., Leon, S., Neri, R., Schinnerer, E., & Tacconi, L. J. 2004, *A&A*, 414, 857
- Crenshaw, D. M., Kraemer, S. B., Hutchings, J. B., Bradley, II, L. D., Gull, T. R., Kaiser, M. E., Nelson, C. H., Ruiz, J. R., & Weistrop, D. 2000, *AJ*, 120, 1731
- Dale, D. A., Sheth, K., Helou, G., Regan, M. W., & Hüttemeister, S. 2005, *AJ*, 129, 2197
- Das, V., Crenshaw, D. M., Hutchings, J. B., Deo, R. P., Kraemer, S. B., Gull, T. R., Kaiser, M. E., Nelson, C. H., & Weistrop, D. 2005, *AJ*, 130, 945
- Davies, R. I., Sánchez, F. M., Genzel, R., Tacconi, L. J., Hicks, E. K. S., Friedrich, S., & Sternberg, A. 2007, *ApJ*, 671, 1388
- de Vaucouleurs, G., de Vaucouleurs, A., Corwin, Jr., H. G., Buta, R. J., Paturel, G., & Fouque, P. 1991, *Third Reference Catalogue of Bright Galaxies*, ed. d. V. A. C. H. G. J. B. R. J. P. G. . F. P. de Vaucouleurs, G.
- Dumas, G., Mundell, C. G., Emsellem, E., & Nagar, N. M. 2007, *MNRAS*, 379, 1249
- Emsellem, E. 2001, in *Astronomical Society of the Pacific Conference Series*, Vol. 249, *The Central Kiloparsec of Starbursts and AGN: The La Palma Connection*, ed. J. H. Knapen, J. E. Beckman, I. Shlosman, & T. J. Mahoney, 91–+
- Englmaier, P., & Shlosman, I. 2000, *ApJ*, 528, 677
- Fernandez, B. R., Holloway, A. J., Meaburn, J., Pedlar, A., & Mundell, C. G. 1999, *MNRAS*, 305, 319
- García-Burillo, S., Combes, F., Eckart, A., Tacconi, L. J., Hunt, L. K., Leon, S., Baker, A. J., Englmaier, P. P., Boone, F., Schinnerer, E., & Neri, R. 2003a, in *Astronomical Society of the Pacific Conference Series*, Vol. 290, *Active Galactic Nuclei: From Central Engine to Host Galaxy*, ed. S. Collin, F. Combes, & I. Shlosman, 423–+
- García-Burillo, S., Combes, F., Hunt, L. K., Boone, F., Baker, A. J., Tacconi, L. J., Eckart, A., Neri, R., Leon, S., Schinnerer, E., & Englmaier, P. 2003b, *A&A*, 407, 485

- García-Burillo, S., Combes, F., Schinnerer, E., Boone, F., & Hunt, L. K. 2005, *A&A*, 441, 1011
- García-Burillo, S., Fernández-García, S., Combes, F., Hunt, L. K., Haan, S., Schinnerer, E., Boone, F., Krips, M., & Márquez, I. 2009, *A&A*, 496, 85
- González Delgado, R. M., Heckman, T., & Leitherer, C. 2001, *ApJ*, 546, 845
- Guilloteau, S., & Lucas, R. 2000, in *Astronomical Society of the Pacific Conference Series*, Vol. 217, *Imaging at Radio through Submillimeter Wavelengths*, ed. J. G. Mangum & S. J. E. Radford, 299–+
- Haan, S., Schinnerer, E., Emsellem, E., García-Burillo, S., Combes, F., Mundell, C. G., & Rix, H. 2009, *ApJ*, 692, 1623
- Heckman, T. M., & Balick, B. 1983, *ApJ*, 268, 102
- Helfer, T. T., & Blitz, L. 1995, *ApJ*, 450, 90
- Hicks, E. K. S., Davies, R. I., Malkan, M. A., Genzel, R., Tacconi, L. J., Sánchez, F. M., & Sternberg, A. 2009, *ApJ*, 696, 448
- Hunt, L. K., Combes, F., García-Burillo, S., Schinnerer, E., Krips, M., Baker, A. J., Boone, F., Eckart, A., León, S., Neri, R., & Tacconi, L. J. 2008, *A&A*, 482, 133
- Hutchings, J. B., Crenshaw, D. M., Kaiser, M. E., Kraemer, S. B., Weistrop, D., Baum, S., Bowers, C. W., Feinberg, L. D., Green, R. F., Gull, T. R., Hartig, G. F., Hill, G., & Lindler, D. J. 1998, *ApJ*, 492, L115+
- Jackson, J. M., Paglione, T. A. D., Ishizuki, S., & Nguyen-Q-Rieu. 1993, *ApJ*, 418, L13+
- Kaiser, M. E., Bradley, II, L. D., Hutchings, J. B., Crenshaw, D. M., Gull, T. R., Kraemer, S. B., Nelson, C. H., Ruiz, J., & Weistrop, D. 2000, *ApJ*, 528, 260
- Knapen, J. H., Stedman, S., Bramich, D. M., Folkes, S. L., & Bradley, T. R. 2004, *A&A*, 426, 1135
- Kohno, K., Ishizuki, S., Matsushita, S., Vila-Vilaró, B., & Kawabe, R. 2003, *PASJ*, 55, L1
- Kohno, K., Kawabe, R., Tosaki, T., & Okumura, S. K. 1996, *ApJ*, 461, L29+
- Krips, M., Eckart, A., Neri, R., Pott, J. U., Leon, S., Combes, F., García-Burillo, S., Hunt, L. K., Baker, A. J., Tacconi, L. J., Englmaier, P., Schinnerer, E., & Boone, F. 2005, *A&A*, 442, 479

- Krips, M., Neri, R., García-Burillo, S., Combes, F., Schinnerer, E., Baker, A. J., Eckart, A., Boone, F., Hunt, L., Leon, S., & Tacconi, L. J. 2007a, *A&A*, 468, L63
- . 2007b, *A&A*, 468, L63
- Leroy, A. K., Walter, F., Brinks, E., Bigiel, F., de Blok, W. J. G., Madore, B., & Thornley, M. D. 2008, *AJ*, 136, 2782
- Lindt-Krieg, E., Eckart, A., Neri, R., Krips, M., Pott, J., García-Burillo, S., & Combes, F. 2008, *A&A*, 479, 377
- Marconi, A., Risaliti, G., Gilli, R., Hunt, L. K., Maiolino, R., & Salvati, M. 2004, *MNRAS*, 351, 169
- Martini, P. 2004, in *IAU Symposium, Vol. 222, The Interplay Among Black Holes, Stars and ISM in Galactic Nuclei*, ed. T. Storchi-Bergmann, L. C. Ho, & H. R. Schmitt, 235–241
- Mundell, C. G., Pedlar, A., Baum, S. A., O’Dea, C. P., Gallimore, J. F., & Brinks, E. 1995, *MNRAS*, 272, 355
- Mundell, C. G., Pedlar, A., Shone, D. L., & Robinson, A. 1999, *MNRAS*, 304, 481
- Mundell, C. G., & Shone, D. L. 1999, *MNRAS*, 304, 475
- Mundell, C. G., Wrobel, J. M., Pedlar, A., & Gallimore, J. F. 2003, *ApJ*, 583, 192
- Onken, C. A., Valluri, M., Peterson, B. M., Pogge, R. W., Bentz, M. C., Ferrarese, L., Vestergaard, M., Crenshaw, D. M., Sergeev, S. G., McHardy, I. M., Merritt, D., Bower, G. A., Heckman, T. M., & Wandel, A. 2007, *ApJ*, 670, 105
- Pedlar, A., Howley, P., Axon, D. J., & Unger, S. W. 1992, *MNRAS*, 259, 369
- Pedlar, A., Kukula, M. J., Longley, D. P. T., Muxlow, T. W. B., Axon, D. J., Baum, S., O’Dea, C., & Unger, S. W. 1993, *MNRAS*, 263, 471
- Penston, M. V., Robinson, A., Alloin, D., Appenzeller, I., Aretxaga, I., Axon, D. J., Baribaud, T., Barthel, P., Baum, S. A., Boisson, C., de Bruyn, A. G., & Clavel, J. 1990, *A&A*, 236, 53
- Perez, E., Gonzalez-Delgado, R., Tadhunter, C., & Tsvetanov, Z. 1989, *MNRAS*, 241, 31P
- Riffel, R., Pastoriza, M. G., Rodríguez-Ardila, A., & Maraston, C. 2007, *ApJ*, 659, L103

- Rigopoulou, D., Papadakis, I., Lawrence, A., & Ward, M. 1997, *A&A*, 327, 493
- Sakamoto, K., Okumura, S. K., Ishizuki, S., & Scoville, N. Z. 1999, *ApJ*, 525, 691
- Schartmann, M., Meisenheimer, K., Klahr, H., Camenzind, M., Wolf, S., & Henning, T. 2009, *MNRAS*, 393, 759
- Schulz, H. 1990, *AJ*, 99, 1442
- Schuster, K. F., Kramer, C., Hitschfeld, M., Garcia-Burillo, S., & Mookerjee, B. 2007, *A&A*, 461, 143
- Sheth, K., Vogel, S. N., Regan, M. W., Thornley, M. D., & Teuben, P. J. 2005, *ApJ*, 632, 217
- Shlosman, I., Frank, J., & Begelman, M. C. 1989, *Nature*, 338, 45
- Solomon, P. M., & Barrett, J. W. 1991, in *IAU Symposium*, Vol. 146, *Dynamics of Galaxies and Their Molecular Cloud Distributions*, ed. F. Combes & F. Casoli, 235–+
- Storchi-Bergmann, T., Lopes, R. D. S., McGregor, P. J., Riffel, R. A., Beck, T., & Martini, P. 2010, *MNRAS*, 402, 819
- Storchi-Bergmann, T., McGregor, P. J., Riffel, R. A., Simões Lopes, R., Beck, T., & Dopita, M. 2009, *MNRAS*, 394, 1148
- Sturm, E., Alexander, T., Lutz, D., Sternberg, A., Netzer, H., & Genzel, R. 1999, *ApJ*, 512, 197
- Tacconi, L. J., Genzel, R., Blietz, M., Cameron, M., Harris, A. I., & Madden, S. 1994, *ApJ*, 426, L77+
- Terlevich, R., Terlevich, E., Portal, M. S., & Diaz, A. I. 1991, *MNRAS*, 249, 36
- Ulrich, M.-H. 2000, *A&A Rev.*, 10, 135
- Usero, A., García-Burillo, S., Fuente, A., Martín-Pintado, J., & Rodríguez-Fernández, N. J. 2004, *A&A*, 419, 897
- Vila-Vilaro, B., Robinson, A., Perez, E., Axon, D. J., Baum, S. A., Gonzalez-Delgado, R. M., Pedlar, A., Perez-Fournon, I., Perry, J. J., & Tadhunter, C. N. 1995, *A&A*, 302, 58

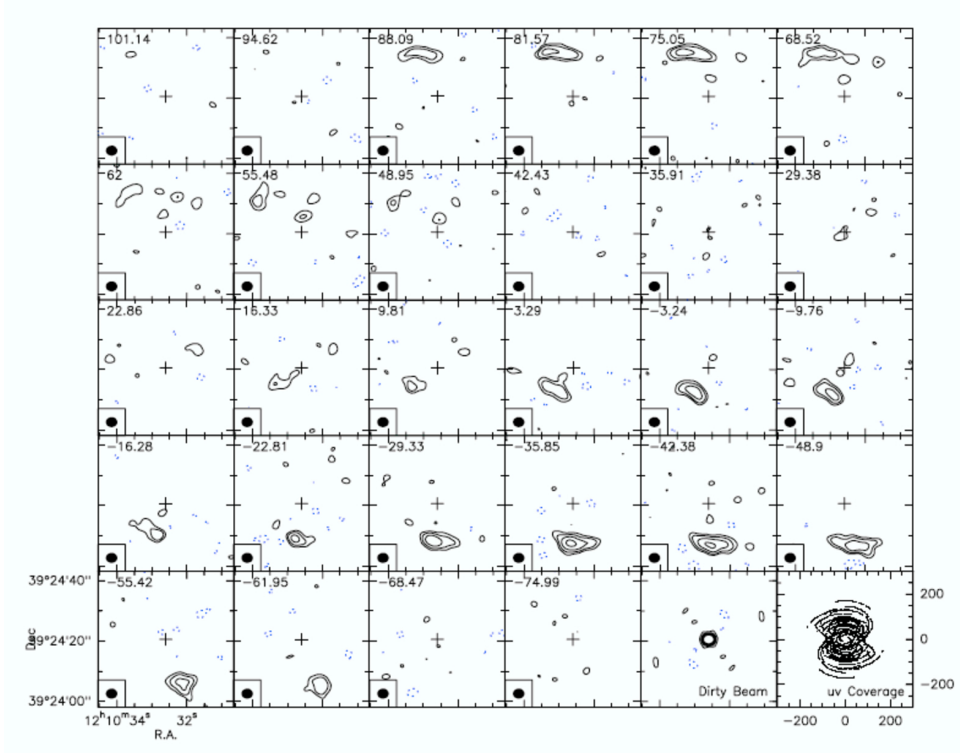


Fig. 1.— Channel maps of the naturally weighted CO(1-0) line emission in NGC4151. The channels are 6.5 km s^{-1} wide and contours are plotted at $-6, -3, 3, 6, 12$ and 24σ with $1\sigma = 2 \text{ mJy beam}^{-1}$. The velocity marking in the top left corner of each panel is relative to the observed central velocity of $v_{sys} = 995 \text{ km s}^{-1}$. The CLEAN beam of $3.44'' \times 2.97''$ is shown in the bottom left corner of each panel. The cross marks the phase center of the observation. The dirty beam and the uv coverage are presented in the last two panels.

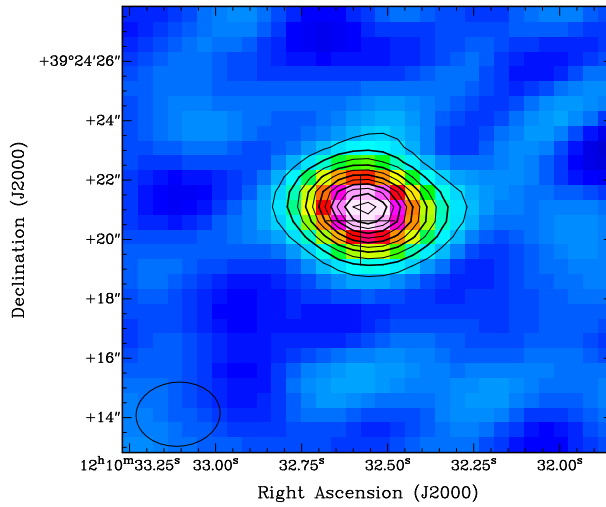


Fig. 2.— 3mm continuum map of NGC4151 using uniform weighting. The beam size of $2.8'' \times 2.2''$ is indicated in the bottom-left corner. The contour levels run from 1 to 12 mJy beam⁻¹ with a step of 1 mJy beam⁻¹ (3.5σ to 43σ in steps of 3.5σ). The cross marks the phase center of the observations, while the peak of the continuum coincides with the location of the AGN, within our astrometric uncertainty.

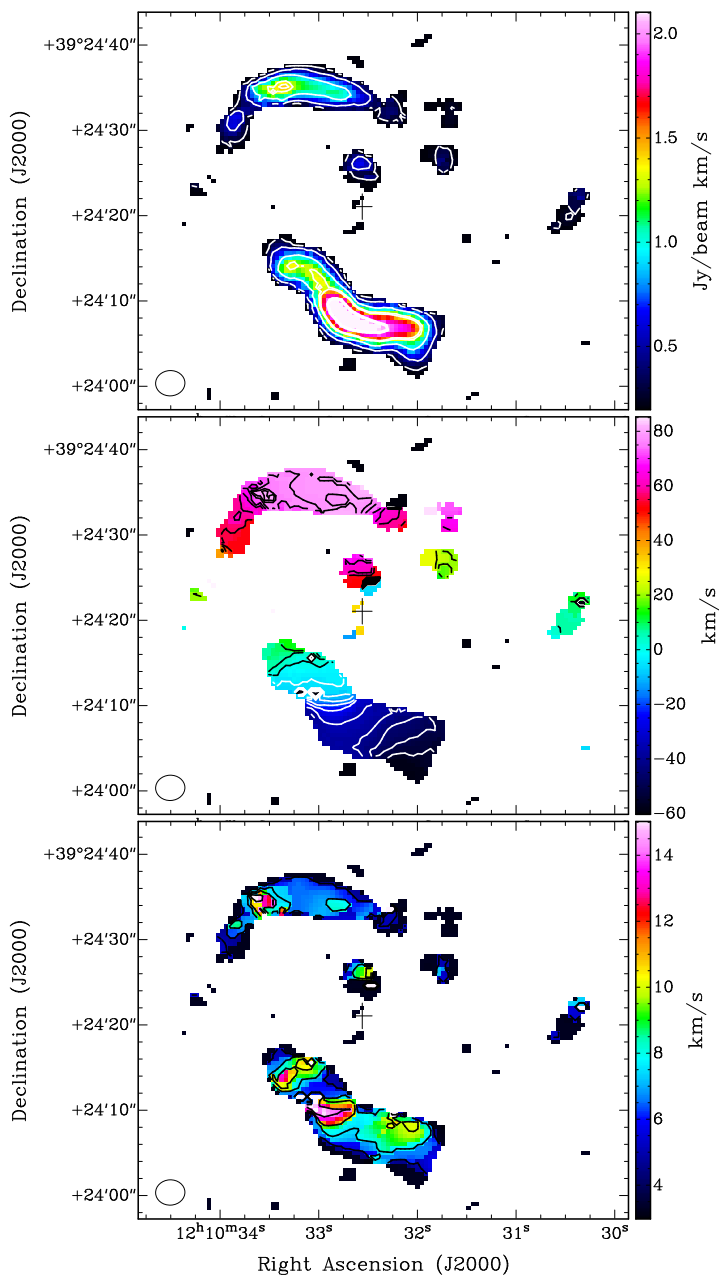


Fig. 3.— Moment maps of the CO(1-0) line emission in NGC 4151: integrated intensity (top), velocity field (middle) and velocity dispersion (bottom). The contour levels are 0.25, 0.5, 0.9, 1.3, 1.5 and 2 Jy beam⁻¹ km s⁻¹ in the intensity map; from -50 km s⁻¹ to 80 km s⁻¹ in steps of 5 km s⁻¹ for the velocity field and 5, 7.5 10 and 14 km s⁻¹ in the dispersion map. The beam size (3.4"×3.0") is shown in the bottom left corner of each panel and the cross marks the location of the AGN as given by its 21cm radio continuum (Mundell et al. 2003).

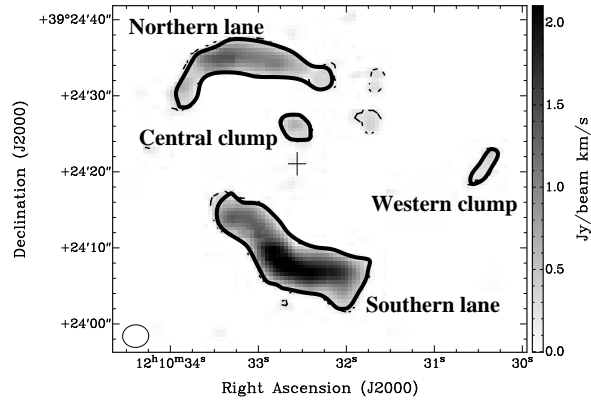


Fig. 4.— The individual components of the CO(1-0) distribution discussed in the text are indicated in the intensity map. The contour marks the $0.21 \text{ Jy beam}^{-1} \text{ km s}^{-1}$ level and roughly outlines the areas used to measure the CO(1-0) line flux for each component (see Table 3).

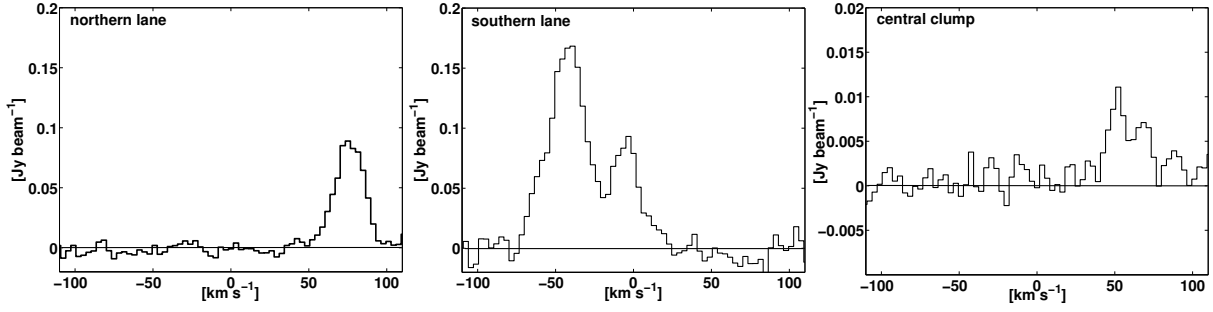


Fig. 5.— Integrated CO spectra of the three major components of the CO distribution: northern gas lane (*left*), southern gas lane (*middle*), and central clump (*right*). For all spectra, the x-axis is relative to the systemic velocity of $v_{sys} = 995 \text{ km s}^{-1}$ (in km s^{-1}) and the y-axis is the integrated flux density in Jy beam^{-1} . Note the second component in the profile of the southern gas lane that is centered at 0 km s^{-1} and mostly arising from the northeastern tip of this lane.

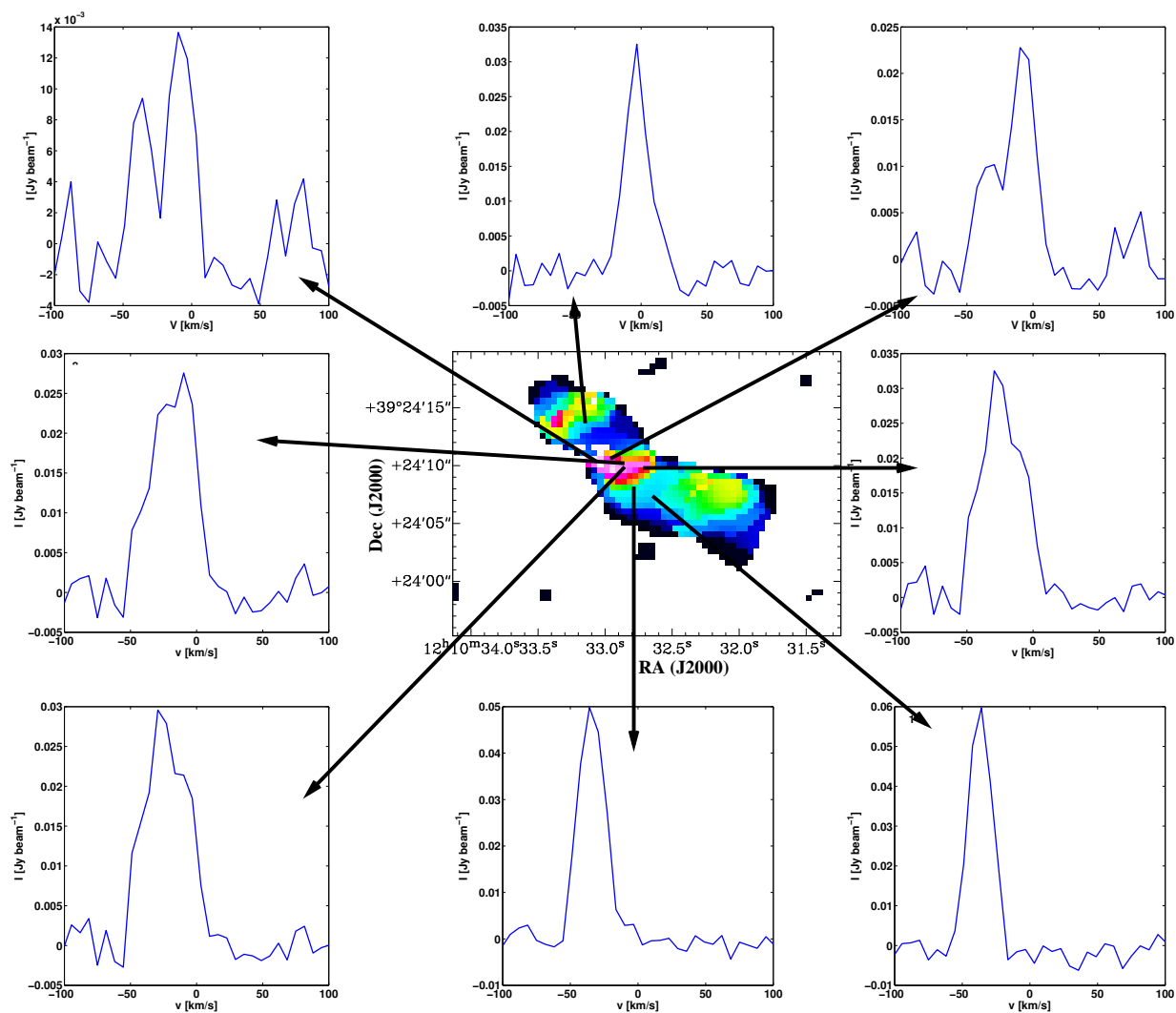


Fig. 6.— CO emission line profiles from different regions of the southern lane. The central panel shows the velocity dispersion across the southern lane, between 3 and 15 km s⁻¹ from blue to white colors. The spectra have been extracted from single pixels of size 0.5'' × 0.5'', the locations of these pixels are indicated by the arrows.

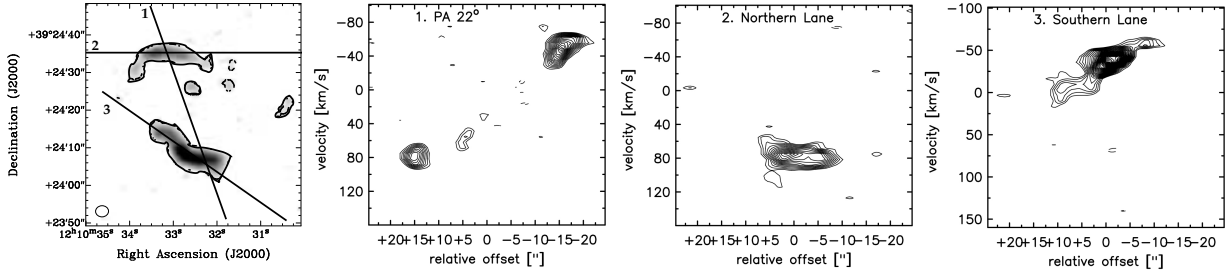


Fig. 7.— CO pv diagrams extracted along several position angles and slits in NGC 4151. Contour levels go from -5σ , -4σ , -3σ , 3σ to 75σ in steps of $1\sigma = 2.8 \text{ mJy beam}^{-1}$. The locations of the slits are indicated in the intensity map (*left*) and the slits are labeled. The pv diagrams shown are along (1): the major kinematic axis (PA= 22°); (2): the northern (PA= 0° , offset= $-7''$; $14''$) and (3): southern (PA= 55° , offset= $-1.5''$; $-13''$) gas lanes (*from left to right*).

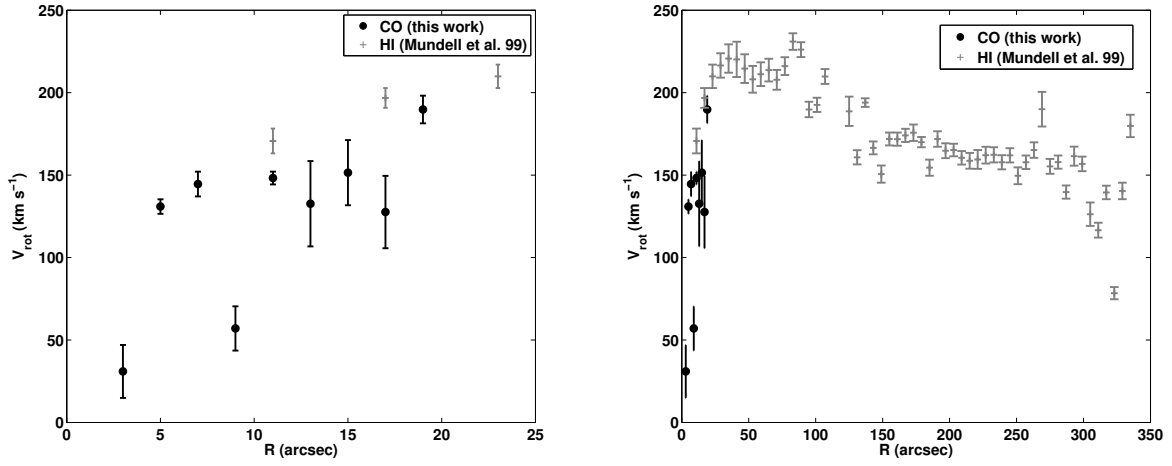


Fig. 8.— Rotation curve of NGC 4151 derived from the CO(1-0) (black circles) and HI velocity fields (gray crosses, from Mundell et al. 1999). Both panels show the combined CO rotation curve (derived with $v_{\text{sys}} = 1010 \text{ km s}^{-1}$) and HI rotation curve, the left panel showing a zoom on the central region. The point at $R=9''$ in CO rotation curve (left panel) corresponds to the north-east part of the southern lane, which has been shown to lie at the systemic velocity (Fig. 5) and appears to be at a lower velocity than expected from circular rotation.

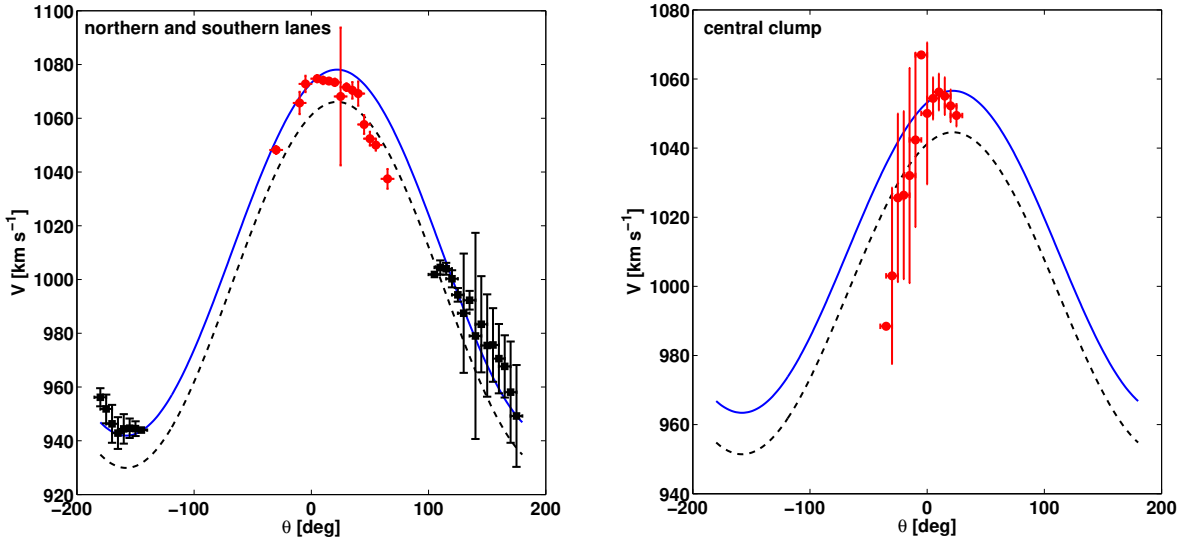


Fig. 9.— *Left*: Velocity along the CO lanes, as a function of position angle θ around the lanes, from north to east. Red circles (respectively black squares) correspond to the northern lane (respectively southern lane). The two curved lines correspond to sinusoids of pure circular velocities for an inclined disk with $\text{PA}=22^\circ$ and $i=21^\circ$ at the major-axis ($18''$) of the gas lanes. *Right*: Velocity within the central clump, as a function of position angle θ , from north to east (red points). The plain and dashed curves corresponds to sinusoids of pure circular velocities with disk orientation of $\text{PA}=22^\circ$ and $i=21^\circ$, at a radius of $5''$, position of the central clump. In both panels, the sinusoids correspond respectively to a systemic velocity of $v_{sys} = 1010 \text{ km s}^{-1}$ (solid blue line), and $v_{sys} = 995 \text{ km s}^{-1}$ (dashed black line).

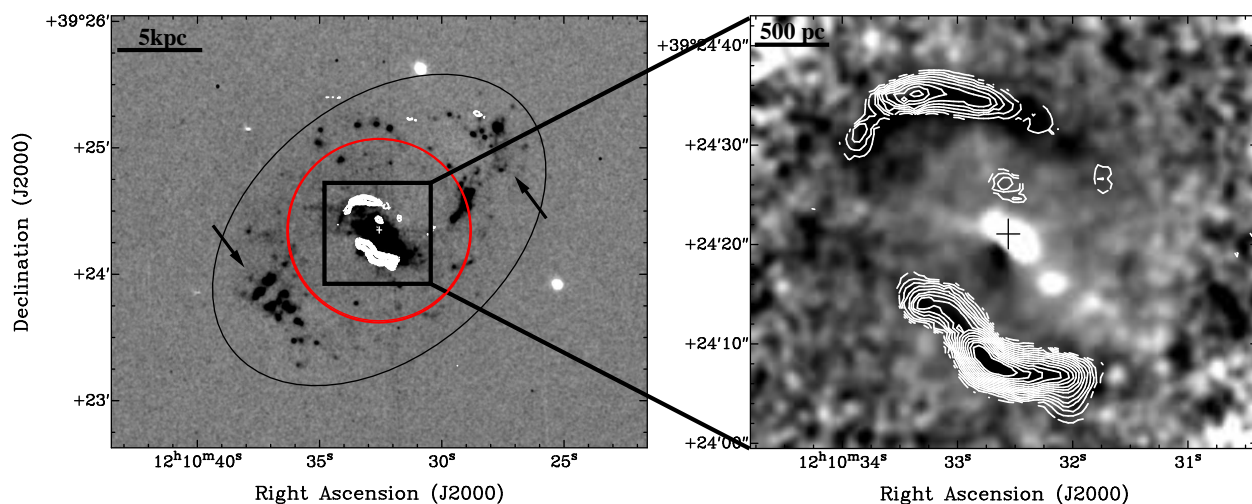


Fig. 10.— CO(1-0) contours overlaid on the H α map (*left*; Knapen et al. 2004) and a V-I color map (*right*; Asif et al. 1998). The ellipse outlines the large-scale stellar bar present in NGC 4151 and the circle corresponds to the position of the ILR as derived by Mundell et al. (1999). Enhanced H α emission is present along the leading sides of the bar (indicated by arrows) that connect to the CO gas lanes. The V-I map was smoothed to 1.5'' resolution to enhance the contrast for the dust lanes. Redder colors are presented by darker shading. The ENLR is evident as the very blue elongated shape in the nucleus. In both panel, the cross marks the position of the AGN.

Table 1. General Properties of NCG 4151

Property	Value	Reference
Right ascension (J2000)	$12^h 10^m 32.^s 58$	Mundell et al. (2003)
Declination (J2000)	$+39^\circ 24' 21'' 06$	Mundell et al. (2003)
Classification	SAB(rs)ab	RC3 (de Vaucouleurs et al. 1991)
AGN Type	Seyfert 1.5	NED
Distance	13.3 Mpc	Mundell et al. (2003)
Scale	$1''=65$ pc	
Systemic Velocity V_{sys}	995 km s^{-1}	Ulrich (2000)
Inclination (i)	21°	Mundell et al. (1999)
Position Angle (PA)	22°	Mundell et al. (1999)
Bar Extent	$3' \times 2'$	Mundell et al. (1999)
Bar PA	130°	Mundell et al. (1999)

Table 2. Dataset Parameters

Dataset	Weighting	Channel Width [km s ⁻¹]	Clean Beam ["×"]	RMS [mJy beam ⁻¹]
continuum	natural	1150.5	3.44×2.96	0.20
continuum	uniform	1150.5	2.83×2.16	0.28
line-only	natural	6.5	3.44×2.96	2.0
line-only	uniform	6.5	2.83×2.16	2.8

Note. — Beam sizes and noise levels of the PdBI continuum maps and line-only data cubes derived at different velocity resolution and weightings.

Table 3. CO Fluxes and Molecular Gas Masses

Component	$S_{CO}dV$ [Jy km s ⁻¹]	M_{mol} [10 ⁷ M _⊙]
Total	14.7	4.3
Southern lane	8.7	2.5
Northern lane	5.0	1.5
Central clump	0.4	0.12
Western Clump	0.63	0.18

Note. — Integrated CO(1-0) line fluxes and corresponding molecular gas masses for different components identified in the CO distribution. The location and extent of the individual components are indicated in Fig. 4. The fluxes have been corrected for primary beam attenuation and the masses include 36% of Helium fraction.